communications materials

A Nature Portfolio journal

Article

https://doi.org/10.1038/s43246-025-00808-0

Superconductivity of zirconium-nitrogen hydrides at megabar pressures

Check for updates

Tao Luo[1,6], Shen-Ao Li[2,3,6], Liu-Cheng Chen[1], Guo-Hua Zhong[2,3] ✉, Hai-Qing Lin[4] & Xiao-Jia Chen[5] ✉

The hydrides based on transition metal nitrides are believed to be potential candidates of low-pressure superconductors. However, the relevant theoretical and experimental studies are lack. Here, we report a theoretical and experimental study of the superconductivity in Zr-N-H system. Two high-pressure phases of $P6_3/mmc$-$ZrNH_2$ and $F\bar{4}3m$-ZrNH are found to be stable. The superconducting transition temperature of the former is theoretically predicted to be relatively low with the values of 15–17 K, while the transition temperature of the latter is higher, close to 40 K at megabar pressures. The difference in transition temperature values mainly comes from the different forms of H in hydrides. To examine this theoretical prediction, we synthesize Zr-N-H ternary hydrides experimentally at high pressures by laser heating. The resistance measurements confirm the superconductivity of $P6_3/mmc$-$ZrNH_2$ and $F\bar{4}3m$-ZrNH. The present results provide a promising avenue for exploring the superconductivity in transition-metal nitrides.

High-temperature superconductors have always been a hot topic in the field of condensed matter physics. Theoretical predictions and experimental studies of several typical binary hydride superconductors indicate that hydrides are potential room-temperature superconductors. For example, in SiH_4, experimental observations of metallization and theoretical predictions of superconductivity are one of the earlier studies on hydride superconductors[1,2]. In hydrides containing H_2 unit, the superconducting transition temperature (T_c) can reach over 100 K[3–5]. In H_3S, high-temperature superconductivity exceeding 200 K was theoretically predicted[6] and experimentally observed[7] for the first time. In LaH_{10} containing clathrate H atom structure, near room temperature superconductivity has been theoretically predicted[8,9] and experimentally confirmed[10,11]. And in CeH_9, the diamagnetism characteristic of the Meissner effect and a sharp drop of the resistance to near zero have been further confirmed[12]. These milestone researches have spurred a significant amount of theoretical and experimental research on binary hydride superconductors[13–24]. Furthermore, exploring more high-temperature superconductivity under low pressure, on the one hand, many in-depth works have been carried out. For example, for the binary hydride LaH_{10}, the structural phase transition from high symmetrical $Fm\bar{3}m$ to low symmetrical $C2/m$ can further reduce the stability pressure to 135 GPa[25]. On the other hand, the research scope needs to be expanded. Multinary hydrides provide a broader research space for finding high-temperature superconductors and offer more potential for discovering room-temperature superconductors[26]. Currently, researchers have shifted their focus to the study of ternary hydrides.

Currently, ternary hydrides can be considered as doping in already synthesized binary hydrides. It may be possible to reduce the pressure required for hydride stability or enhance the T_c by introducing additional elements. Based on this idea, numerous theoretical calculations have focused on doping high-T_c binary hydrides to form ternary hydrides, including three types of nonmetal-nonmetal-hydrogen, metal-metal-hydrogen, and metal-nonmetal-hydrogen. For nonmetal-nonmetal-hydrogen-like, most theoretical studies were based on the H_3S system for doping other elements[27–30]. In some of these ternary hydrides, the T_c can be optimized and increased. However, few successful experimental verifications have been reported. For metal-metal-hydrogen system, researchers have designed novel ternary hydrides based on prototype structures of CaH_6, CeH_9, and LaH_{10}. These designs aim to optimize superconducting properties through interactions and doping effects between elements. Significant progress has been made in experimental research on metal-metal-hydrogen systems. For example, ternary alloy hydrides such as (La, Y)H_6 (T_c = 237 K at 176 GPa)[31], (La, Y)H_{10} (T_c = 253 K at 183 GPa)[31], (La, Ce)H_9 (T_c = 173 K at 110 GPa)[32,33], (Y, Ce)H_9 (T_c = 140 K at 120 GPa)[34], and (La, Ce)H_{10} (T_c = 175 K at 155 GPa)[35] have been synthesized, further enriching the family of high-temperature superconductors. For metal-nonmetal-hydrogen ternary

[1]School of Science, Harbin Institute of Technology, Shenzhen, China. [2]Shenzhen Institutes of Advanced Technology, Chinese Academy of Sciences, Shenzhen, China. [3]University of Chinese Academy of Sciences, Beijing, China. [4]School of Physics, Zhejiang University, Hangzhou, China. [5]Department of Physics and Texas Center for Superconductivity, University of Houston, Houston, TX, USA. [6]These authors contributed equally: Tao Luo, Shen-Ao Li.
✉e-mail: gh.zhong@siat.ac.cn; xjchen@uh.edu

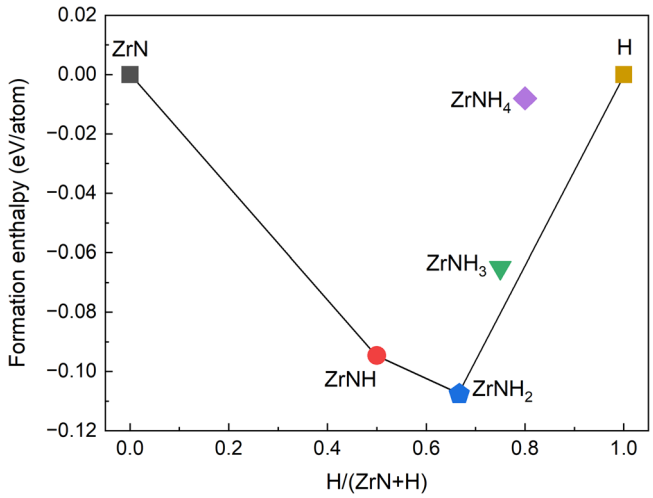

Fig. 1 | Phase diagram. Convex hull diagram for the Zr-N-H system with respect to ZrN and H at 140 GPa.

system, which has attracted much attention, numerous structures have been theoretically designed to explore the stability below 100 GPa, such as clathrate $LaBH_8$[36,37] and molecular crystal MB_2H_8 (M = K, Rb, and Cs)[38,39] and MC_2H_8 (M = Na, K, Mg, Al, and Ga)[40]. Theoretical predictions suggest that the metal-nonmetal-hydrogen ternary system can achieve higher T_c below 100 GPa, even as low as a few dozen GPa, but there is a lack of relevant experimental verification. Metal-nitrogen-hydrogen is another recently highly anticipated metal-nonmetal-hydrogen system, such as Lu-N-H. However, the superconductivity of Lu-N-H is highly questionable. The absence of the near ambient-pressure room-temperature superconductivity of Lu-N-H has been well supported by experiments[41] and high-throughput theoretical calculations[42]. But, superconducting phases are allowed at high pressures although the critical temperatures are far below the room temperature, such as the experimental studies[43] and the theoretical predictions[42]. Additionally, in the MN_2H_8 (M = Al, Mg, Ga, Zn, Cd, and Hg) system, it was predicted that there would be ambient or low-pressure superconductivity[44]. This indicates that compounds composed of nitrogen and hydrogen may exhibit unusual physical properties under high pressure. The existence or absence of superconductivity in metal nitrogen hydrides is worth further exploration.

Transition metal nitrides (TMNs) are interstitial compounds that can accommodate other elements into their lattices. The crystal structure, dynamical properties, and superconductivity of TMNs such as TiN, ZrN, HfN, and NbN have been widely reported in numerous studies[45–51]. However, research on the hydrides based on TMNs is still quite lacking; especially their superconductivity needs further exploration and confirmation. Among TMNs, ZrN has rich properties such as structural phase transition under pressure, superhardness, and superconductivity[49,51–54]. In this study, therefore, we have selected ZrN as the precursor material to explore the crystal structures, electronic characteristics, and possible superconductivity of Zr-N-H ternary hydrides and further synthesized the Zr-N-H ternary hydrides at megabar pressure. We predicted two novel Zr-N-H ternary hydrides of $P6_3/mmc$-$ZrNH_2$ with T_c in 15–17 K and $F\bar{4}3m$-ZrNH with T_c in 36–40 K, respectively, and the obtained T_c values of the two kinds of Zr-N-H systems based on the resistance measurements are consistent with the theoretical results.

Results and Discussion

Theoretical prediction

In order to focus on the research scope, we fixed the Zr:N ratio at 1:1, which means that the form of Zr-N-H ternary hydride is $ZrNH_x$. Then, we used particle swarm optimization algorithm to search for the low-enthalpy structures of $ZrNH_x$ (x = 1, 2, 3, 4) in the pressure range of 100–150 GPa and predicted the superconducting parameters of stable structures within the framework of electron-phonon coupling (EPC) theory. For each chemical ratio (each hydrogen content), we chose the structure with the lowest enthalpy to calculate the total energy, and then compared it with the energies of ZrN and hydrogen to obtain the enthalpy of formation. As shown in Fig. 1, the enthalpy of formation of $ZrNH_x$ relative to ZrN and H at a pressure of 140 GPa is presented in convex hull form, where the $C2/c$ structure of H_2[55] and the CsCl-type structure of ZrN[56] were adopted. We found two Zr-N-H ternary hydrides are thermodynamically stable, namely $ZrNH_2$ with $P6_3/mmc$ space-group and ZrNH with $F\bar{4}3m$ space-group. Neither of these structures is considered a high H content system. $Cmcm$-$ZrNH_3$ and P-$4m2$-$ZrNH_4$ with relatively high hydrogen content are thermodynamically metastable, 0.016 eV/atom and 0.055 eV/atom above the hull energy, respectively.

For thermodynamically stable phases of Zr-N-H, Fig. 2 shows the crystal structures of $P6_3/mmc$-$ZrNH_2$ and $F\bar{4}3m$-ZrNH. It is found that hydrogen element exists in the form of quasi H_2 molecules in $P6_3/mmc$-$ZrNH_2$, while hydrogen element exists in the atom-like form, bonding with Zr atoms in $F\bar{4}3m$-ZrNH. As shown in Fig. 2, in $F\bar{4}3m$-ZrNH, Zr and N maintain the NaCl-type structural characteristics of ZrN[52], and the H atoms occupy the tetrahedral interstices. In $P6_3/mmc$-$ZrNH_2$, the structural characteristics of Zr and N are different from both NaCl-type ZrN and CsCl-type ZrN. The coordination number of N to Zr becomes 5, and the quasi H_2 molecules formed by H atoms are arranged along the c-axis direction. Figure 2a, b shows the volume, lattice parameters, and bonding lengths in two hydrides as a function of pressure. As the pressure changes, these crystal parameters show continuity. As expected, the volume decreases significantly with increasing pressure. Except for the H-H bond length in quasi H_2 molecules, other bond lengths, such as Zr-N and Zr-H, decrease with increasing pressure, but the H-H bond length remains almost unchanged. For $P6_3/mmc$-$ZrNH_2$, Zr atom is at Wyckoff 2c site, N atom is at Wyckoff 2d site, while H atom is at Wyckoff 4e site. At 150 GPa, the lattice parameters of $P6_3/mmc$-$ZrNH_2$ are $a = b = 3.465$ Å and $c = 4.125$ Å. The H-H bond length d_{H-H} in quasi H_2 molecule is 0.885 Å, and the distance d_{Zr-N} between Zr and N is 2.000 Å or 2.062 Å. With regard to $F\bar{4}3m$-ZrNH, Zr atom is at Wyckoff 4b site, N atom is at Wyckoff 4a site, while H atom is at Wyckoff 4c site. At 145 GPa, the lattice parameters of $F\bar{4}3m$-ZrNH are $a = b = c =$ 4.246 Å. The bond lengths of d_{Zr-H} and d_{Zr-N} are 1.839 Å and 2.123 Å, respectively. To further understand the structural characteristics of these two ternary hydrides, we have also presented the calculated X-ray diffraction patterns of $P6_3/mmc$-$ZrNH_2$ (Fig. 1c) and $F\bar{4}3m$-ZrNH (Fig. 1d), respectively.

Within the considered pressure range, we selected typical pressure points and calculated the band structure along high-symmetrical k-point paths and density of states (DOS), including total and projected on elements. Figure 3a, b shows the electronic structures $P6_3/mmc$-$ZrNH_2$ at 150 GPa and $F\bar{4}3m$-ZrNH at 145 GPa, respectively. From the band structures, both $P6_3/mmc$-$ZrNH_2$ and $F\bar{4}3m$-ZrNH exhibit the obvious metallic characteristics under pressure. Two bands cross the Fermi level in $P6_3/mmc$-$ZrNH_2$ at 150 GPa, while seven bands cross the Fermi level in $F\bar{4}3m$-ZrNH at 145 GPa, forming the complex Fermi surfaces. The electronic DOS at the Fermi level indicates that $F\bar{4}3m$-ZrNH has a higher total DOS value than $P6_3/mmc$-$ZrNH_2$, the former is about 0.173 states/eV/atom, while the latter is about 0.095 states/eV/atom. The values of DOS at the Fermi level are comparable with other hydrides containing H_2 molecules[4] and SH_3[6], but less than those of several metal superhydrides such as LaH_{10}[8] and TbH_{10}[17]. From the perspective of electronic DOS, Zr has the greatest contribution to the electronic DOS at the Fermi level, followed by H, and N has the smallest contribution.

Choosing the same pressure, we have calculated phonon dispersion, phonon density of states (PhDOS), and Eliashberg spectra function $\alpha^2F(\omega)$ to understand the superconductivity of $P6_3/mmc$-$ZrNH_2$ and $F\bar{4}3m$-ZrNH. Figure 3 shows the results $P6_3/mmc$-$ZrNH_2$ at 150 GPa and $F\bar{4}3m$-ZrNH at 145 GPa. The absence of phonon imaginary frequencies proves that these

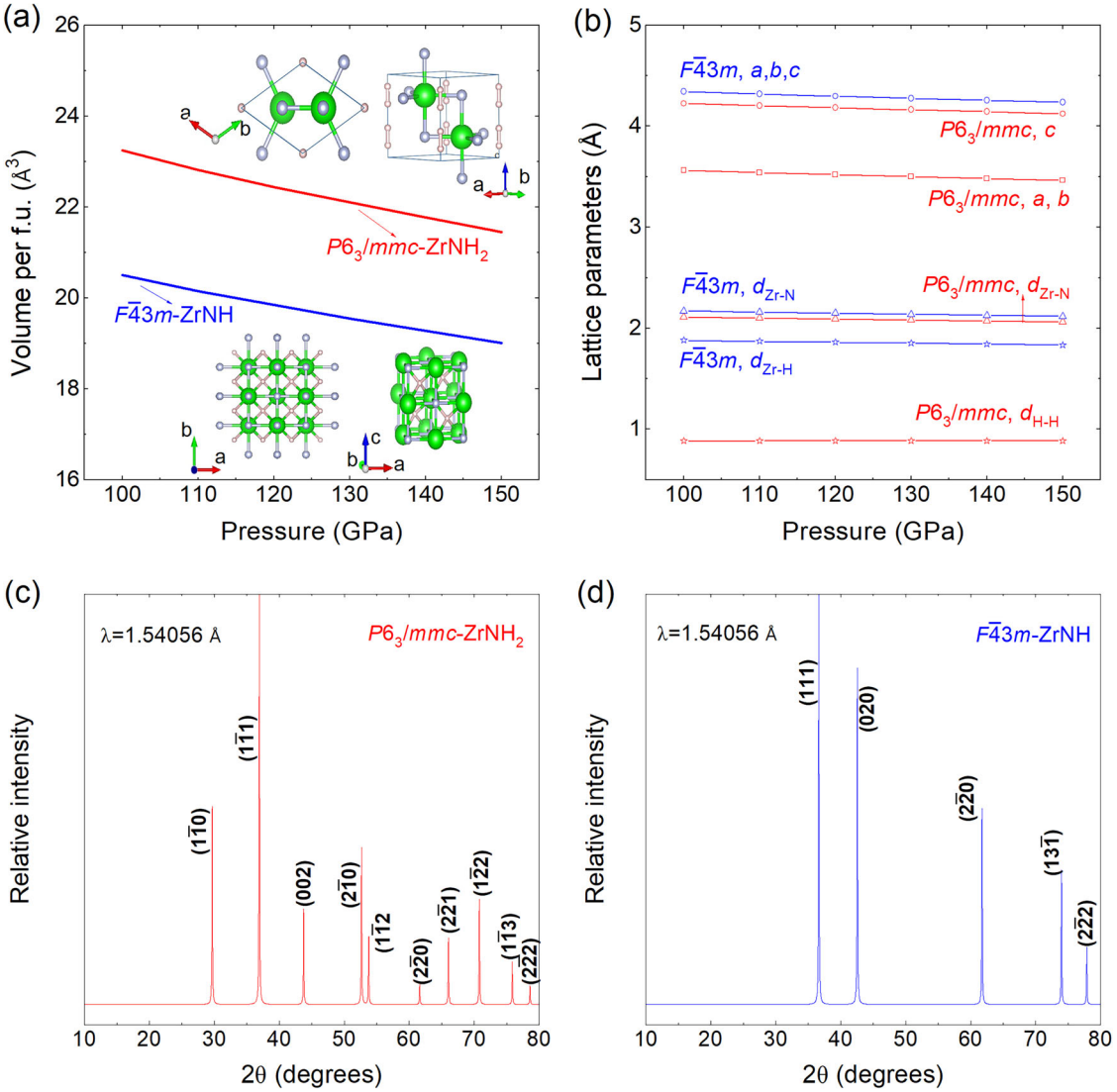

Fig. 2 | Crystal structural parameters of $P6_3/mmc$-$ZrNH_2$ and $F\bar{4}3m$-ZrNH. **a** Volume of hydrides of $P6_3/mmc$-$ZrNH_2$ and $F\bar{4}3m$-ZrNH as a function of pressure. Inset: The crystal structures of $P6_3/mmc$-$ZrNH_2$ and $F\bar{4}3m$-ZrNH viewed from different directions. Green, silver, and pink balls represent Zr, N, and H atoms, respectively. **b** Lattice parameters of $P6_3/mmc$-$ZrNH_2$ and $F\bar{4}3m$-ZrNH as a function of pressure, including lattice constants (**a**, **b**, **c**), bonding lengths between Zr and N (d_{Zr-N}), between Zr and H (d_{Zr-H}), and between H and H (d_{H-H}). **c**, **d** are the calculated X-ray diffraction patterns of $P6_3/mmc$-$ZrNH_2$ and $F\bar{4}3m$-ZrNH, respectively.

two hydrides satisfy the dynamic stability. Neglecting the small differences in pressure, the presence of quasi H_2 molecules in $P6_3/mmc$-$ZrNH_2$ leads to higher phonon vibration frequencies as shown in Fig. 4a and d. Combining phonon spectra with the PhDOS projected on atoms, we find that, in $P6_3/mmc$-$ZrNH_2$, the vibration modes contributing in the frequency range of 1850–2560 cm^{-1} mainly result from H-H stretching vibration in H_2 units, the phonon frequency in the range of 1200–1550 cm^{-1} comes from the attraction of N atoms to H_2 molecules, or the coupling vibration between H_2-H_2, and the vibration frequencies of N and Zr are concentrated in the range of 600–900 cm^{-1} and below 400 cm^{-1}, respectively. The Raman active mode (A_g and B_{3g}) and infrared active mode (B_{2u}, A_u, and B_{3u}) at the Brillouin zone center are labeled for $P6_3/mmc$-$ZrNH_2$, and the Raman active mode (A_1) and Raman + infrared active mode (T_1 and T_2) at the Brillouin zone center are also labeled for $F\bar{4}3m$-ZrNH. The attraction of Zr to H atom in $F\bar{4}3m$-ZrNH is stronger than that of N to H_2 molecules in $P6_3/mmc$-$ZrNH_2$, resulting in a slight increase in the vibration frequency of H in $F\bar{4}3m$-ZrNH. Similarly, N also experiences a slight decrease in frequency due to the relatively big Zr-N distance in $F\bar{4}3m$-ZrNH. As a result, phonon bandwidths are relatively smaller in $F\bar{4}3m$-ZrNH than those of $P6_3/mmc$-$ZrNH_2$.

Although there is a wider phonon frequency range in $P6_3/mmc$-$ZrNH_2$, there is a stronger PhDOS (Fig. 4b, e) and Eliashberg spectra function (Fig. 4c, f) in $F\bar{4}3m$-ZrNH. Hence, a larger EPC constant is obtained in $F\bar{4}3m$-ZrNH, as shown in Fig. 4c, f. The total EPC constants are 0.95 for $P6_3/mmc$-$ZrNH_2$ at 150 GPa and 1.32 for $F\bar{4}3m$-ZrNH at 145 GPa, respectively. The logarithmic average of phonon frequency (ω_{log}) is 327.6 K and 384.7 K in $P6_3/mmc$-$ZrNH_2$ and $F\bar{4}3m$-ZrNH, respectively. Neither of these structures is considered a high H content system, so when we used the Allen-Dynes-corrected McMillan eq.[57] to calculate the superconducting transition temperature, we took 0.15 for the Coulomb pseudopotential μ^*. Combining the calculated λ and ω_{log} with $\mu^* = 0.15$, we can obtain that the T_c is 17.1 K for $P6_3/mmc$-$ZrNH_2$ at 150 GPa and 36.1 K for $F\bar{4}3m$-ZrNH at 145 GPa, respectively. Although H's contribution to the total EPC is relatively small in these two ternary hydrides, $F\bar{4}3m$-ZrNH leads to a stronger ω_{log} than $P6_3/mmc$-$ZrNH_2$, which further increases T_c in Zr-N-H system.

To understand the superconductivity of these two Zr-N-H hydrides, we have calculated the T_c of ZrN under high pressure. We found that the theoretically predicted $T_c = 3.9$ K of ZrN at 145 GPa is obviously different from the superconducting transition temperatures of Zr-N-H. The presence of quasi H_2 molecules has a positive effect on enhancing the

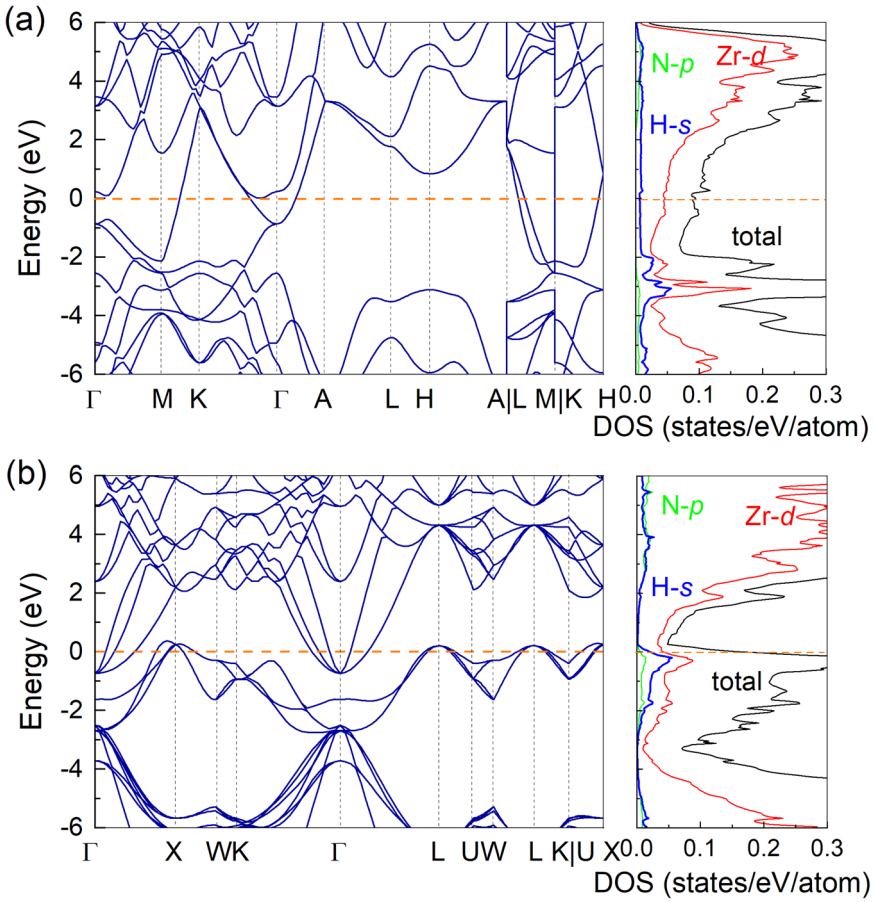

Fig. 3 | Electronic structures of $P6_3/mmc$-$ZrNH_2$ and $F\bar{4}3m$-ZrNH. Band structure along high-symmetrical k-point paths and density of states (DOS) including total and projected on elements. **a** and **b** are corresponding to $P6_3/mmc$-$ZrNH_2$ at 150 GPa and $F\bar{4}3m$-ZrNH at 145 GPa, respectively.

superconductivity of hydrides[3–5,58], which is why $P6_3/mmc$-$ZrNH_2$ exhibits slightly stronger superconductivity than ZrN. $F\bar{4}3m$-ZrNH has higher T_c than $P6_3/mmc$-$ZrNH_2$, implying that the approximate quasi H atomic form further enhances the superconductivity of hydrides, which has been further confirmed in other cage hydrides[8,9,13–18,59,60]. Due to the relatively small contribution of hydrogen to the DOS value at the Fermi level, these two Zr-N-H hydrides exhibit the lower superconducting transition temperature lower than H_3S and LaH_{10}.

Expanding to other pressures within the range of 100–150 GPa, we observed the variation of superconducting parameters of $P6_3/mmc$-$ZrNH_2$ and $F\bar{4}3m$-ZrNH with pressure and summarized in Table 1. Figure 5 also shows the superconducting transition temperature of these two hydrides as a function of pressure. We can further observe that the T_c's of the two hydrides are different from that of ZrN throughout the entire pressure range, and the T_c's of the two hydrides are also significantly different. Although the T_c of the two hydrides fluctuates slightly with pressure changes, they are basically maintained at the same level. The T_c of $ZrNH_2$ is in the range of 15–17 K within the considered pressure range, while the T_c of ZrNH varies in the range of 36–40 K with pressure changes. As shown in Table 1, $F\bar{4}3m$-ZrNH has stronger electron-phonon interactions than $P6_3/mmc$-$ZrNH_2$, but the EPC strengths of these two hydrides are still at a moderate level, lower than those of hydrides with high T_c[6,13–17].

Experimental preparation and measurement

Based on the theoretical prediction of the superconductivity of Zr-N-H ternary hydrides, we have attempted the experimental synthesis at high pressures and laser heating conditions. ZrN with NaCl-type structure was pressed into small pieces and loaded together with ammonia borane (NH_3BH_3) into diamond anvil cell (DAC). NH_3BH_3 was selected as the hydrogen source due to its decomposition reaction upon heating[11]. Due to the enormous challenges of high-pressure experiments, we only demonstrate the superconductivity of predicted hydrides based on the electrical transport measurements through the realization of the zero-resistance state. We started the experiments at pressures from 30 GPa on because of the existence of pressure for the pressed sample in the sample chamber between the small-size diamond anvils. To study the conductivity behavior of the ternary hydride Zr-N-H, we prepared two kinds of samples of ZrN and Zr-N-H, namely, without and with H produced by NH_3BH_3.

We first observed the conductivity of ZrN under pressure without hydrogen source. ZrN was compressed to 145 GPa. The inset of Fig. 6a shows an optical microscope image of the sample ZrN placed on an insulating c-BN cushion with four Pt wires. Figure 6a displays the temperature dependence on the resistance of the sample ZrN from 2 to 300 K at pressures up to 145 GPa. At a pressure of 104 GPa, the resistance at normal state shows the metallic behavior with a decreasing resistance as the temperature decreases. However, when the pressure reaches 114 GPa, the resistance at normal state of ZrN exhibits the non-metallic behavior with increasing resistance as the temperature decreases. As the pressure further increases, the non-metallic behavior of the resistance at normal state is gradually suppressed. The sudden change in the resistance at normal state of ZrN around 110 GPa may be attributed to a phase transition of the sample. Figure 6b is an enlarged view of the low-temperature region of Fig. 6a, showing a temperature range from 0 to 10 K. It can be seen that the T_c of ZrN is relatively low ~5 K over a pressure range from 104 to 145 GPa, which is comparable with the predicted result of 3.9 K at 145 GPa. The T_c values of ZrN at high pressures are lower than 10.7 K at ambient pressure[52], and its underlying mechanism is still unclear. One possible reason is that the crystal structure of ZrN has been changed under pressure, which needs to be further explored in future study.

In the second set of experiments, ZrN and NH_3BH_3 were placed in the DAC. As shown in Fig. 6c, the Zr-N-H samples were synthesized by the laser heating at temperature of about 1600 K and at pressure of about 100 GPa.

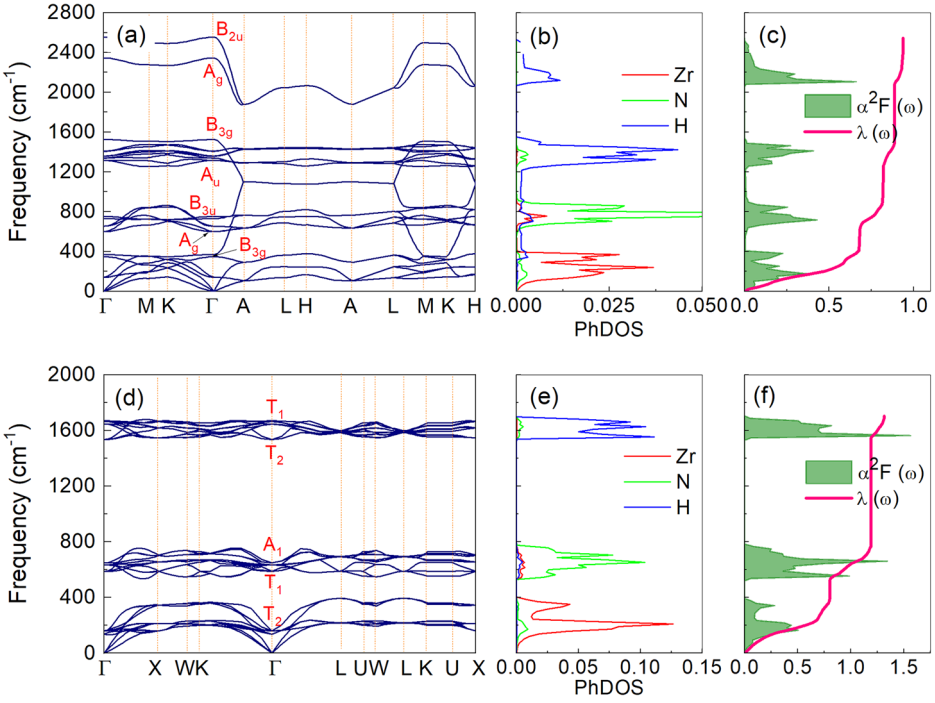

Fig. 4 | Phonon structures and superconducting parameters of $P6_3/mmc$-$ZrNH_2$ and $F\bar{4}3m$-ZrNH. Phonon spectra, phonon density of states (PhDOS) projected on atoms, Eliashberg spectral function $\alpha^2F(\omega)$, and electron-phonon coupling integral $\lambda(\omega)$. **a**–**c** correspond to $P6_3/mmc$-$ZrNH_2$ at 150 GPa, and (**d**–**f**) correspond to $F\bar{4}3m$-ZrNH at 145 GPa. The Raman active mode (A_g and B_{3g}) and infrared active mode (B_{2u}, A_u, and B_{3u}) at the Brillouin zone center are labeled for $P6_3/mmc$-$ZrNH_2$, and the Raman active mode (A_1) and Raman + infrared active mode (T_1 and T_2) at the Brillouin zone center are also labeled for $F\bar{4}3m$-ZrNH.

Table 1 | Calculated superconducting parameters

System	Pressure (GPa)	λ	ω_{log} (K)	T_c (K, μ = 0.15)
	100	0.88	397.5	17.2
	110	0.87	389.2	15.5
$P6_3/mmc$-$ZrNH_2$	120	0.84	390.8	15.0
	130	0.86	381.4	15.6
	140	0.85	358.2	15.8
	150	0.95	327.6	17.1
	100	1.11	563.8	39.6
	110	1.13	533.4	38.7
	120	1.18	519.1	40.8
$F\bar{4}3m$-ZrNH	130	1.17	494.3	38.4
	142	1.29	431.4	39.2
	145	1.32	384.7	36.1
	150	1.20	460.8	37.4

The EPC constant *lambda*, the logarithmic average of phonon frequency ω_{log}, and the superconducting transition temperature T_c of $P6_3/mmc$-$ZrNH_2$ and $F\bar{4}3m$-ZrNH at different pressures.

The temperature dependence of the resistance was then measured in the pressure range of 100–151 GPa. After laser heating, the resistance of the sample exhibits the metallic behavior. The results at 100 GPa and 130 GPa are missing in the high-temperature region due to a lack of counting during the cooling process in the cryostat. However, this does not affect the determination of the superconducting transition temperature in the low-temperature region. As the pressure increases, the resistance of the sample gradually decreases. Generally, the resistivity is related to carrier concentration and mobility. Under pressure, the mobility usually decreases, so the decrease in resistivity under pressure is mainly due to the increase in the carrier concentration. The inset of Fig. 6c shows a picture of Zr-N-H sample in DAC. The bright areas are *c*-BN, while the dark areas are Pt electrodes. Due to the fact that the samples shown in Figs. 6a, 5c were measured in different DACs, a comparison of the normal state resistance is needed. Figure 6d shows an enlarged view of the low-temperature region of Fig. 6c, highlighting the superconducting transition temperature of the sample after laser heating. At 100 GPa, the T_c is 13 K, which is obviously different from the 5 K of ZrN shown in Fig. 6b, indicating that ZrN reacted with hydrogen to form a ternary hydride. After the reaction at 100 GPa is completed, the resistance drop of Zr-N-H is relatively sharp with a narrow superconducting transition width, likely due to quasi-hydrostatic pressure in the sample chamber as NH_3BH_3 releases hydrogen. As the pressure increases, the superconducting transition width of Zr-N-H gradually increases due to pressure gradients in the sample chamber. It is clear from Fig. 6d that as the pressure increases, the superconducting transition temperature increases as well. When the pressure reaches 151 GPa, it appears to be approaching an upper limit.

At a pressure of 151 GPa, we conducted the second laser heating experiment, which lasted longer than the first run. After heating, we performed electrical transport measurements and obtained the resistance-temperature behavior, as shown in the purple line in Fig. 6e. From the resistance curve, it can be seen that the resistance at the normal state of the sample still exhibits metallic behavior. However, comparing with the resistance value at normal state after the first laser heating, the resistance value at the normal state is almost doubled after the second heating. The positive normal resistance changes indicate that the sample undergoes some changes. In addition, the temperature at which the resistance value changed changes significantly after the second heating. According to Fig. 6d, the T_c at 151 GPa is ~15 K. However, Fig. 6f shows that the temperature at which the resistance drops sharply after the second heating is ~33 K. These changes suggest that the sample undergoes some changes, resulting in changes in the resistance at the normal state and the temperature at which the resistance changes. However, since the zero resistance state is not achieved, it cannot be entirely determined if this is a superconducting feature. Therefore, we continued to perform the third heating experiment on the sample.

In the third heating experiment, we increased the laser power and heating time to ensure full reaction of the sample. After heating, we found that the pressure in the sample chamber decreased. Observed through an optical microscope, as shown in Fig. 6e, we found the circular cracks and damage on the surface of the diamond, which was the cause of the pressure drop in the sample chamber. The inset still shows that the structure of the sample chamber is consistent with Fig. 6c, indicating that the diamond

cracks did not affect the sample and electrode, only changing the pressure. Then, the electrical transport measurements were carried out, and the blue curve in Fig. 6e shows the measurement results. Before the transport measurements, we examined the pressure and found it to be 142 GPa. The resistance at the normal state after the third heating still shows metallic behavior, with a decrease in resistance as the temperature is decreased. Comparing with the first and second heating runs, the resistance at the normal state decreases significantly, ~0.1 Ω, as shown in Fig. 6e. In addition to the changes in the resistance at the normal state, the transition temperature also changes. It increases from 33 K in the second heating to 38–39 K in the third heating, and as shown in Fig. 6f. Most importantly, the zero resistance has been achieved at this time. The appearance of the zero-resistance state indicates that a complete superconducting channel has been formed in the synthesized sample. As the pressure increases further, the superconducting transition temperature gradually decreases, which is different from the trend obtained during the second heating run. Especially, the temperature at which the zero-resistance was reached is higher than the transition temperature during the second heating run, so we believe this is a new type of hydrogen-bearing compound. The superconducting transition temperature is highed this time, compared to those of the ternary hydride observed during the second heating run. We thus speculate that a different ternary hydride phase has been formed at the complete heating conditions.

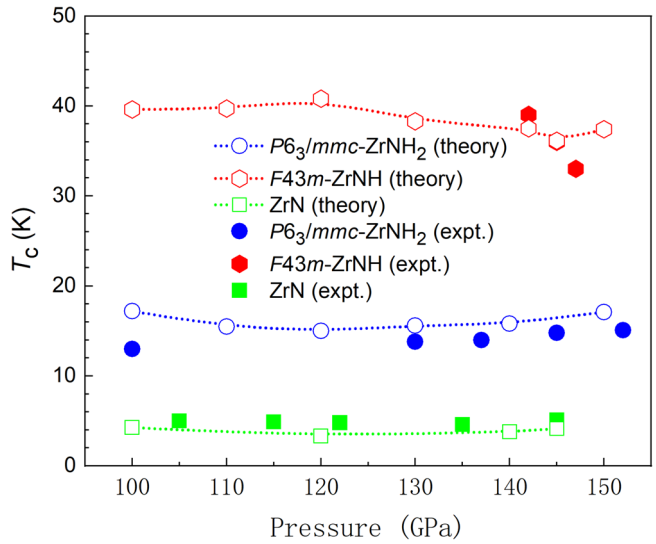

Fig. 5 | Pressure dependence on T_c for ZrN, $P6_3/mmc$-ZrNH$_2$ and $F\bar{4}3m$-ZrNH. Theoretical predictions and experimental results are represented by hollow and solid symbols, respectively.

From these experimental efforts of sample synthesis as well as the electrical transport measurements, we are able to compare the experimentally and theoretically obtained T_c results along their evolution with pressure for ZrN and Zr-N-H in Fig. 5. Visibly, the change of T_c with pressure indicates that there are three superconducting systems. The one with the lowest T_c is ZrN. Within the pressure range from 100 to 150 GPa, the measured T_c of ZrN remains nearly constant at around 5 K (theoretically predicted ~4 K). The first laser heating process resulted in the generation of the second superconducting system. As shown in Fig. 5, the T_c of the second superconducting system was characterized to about 13 K at 100 GPa and gradually increased with increasing pressure, reaching about 15 K at 151 GPa. The T_c of the second superconducting system is evidently different from that of the first superconducting system (ZrN), which implies the generation of Zr-N-H ternary hydride. By comparing with theoretical results, we suggest that the second superconducting system is $P6_3/mmc$-ZrNH$_2$.

The third heating process resulted in the formation of the third superconducting system. The T_c of the third superconducting system was characterized to about 39 K at 142 GPa. As the pressure increased, T_c of the third superconducting system decreased to about 33 K at 147 GPa. As shown in Fig. 5, the T_c of the third superconducting system is significantly higher than that of the second superconducting system. The results indicate that a ternary hydride differing from $P6_3/mmc$-ZrNH$_2$ generates. Combining with the theoretical and experimental results, we can point out that the third superconducting system is $F\bar{4}3m$-ZrNH. Thus, we have obtained the consistent results from both the experimental and experimental aspects. The Zr-N-H ternary hydride superconductors are theoretically predicted and experimentally realized. The superconducting transition temperature

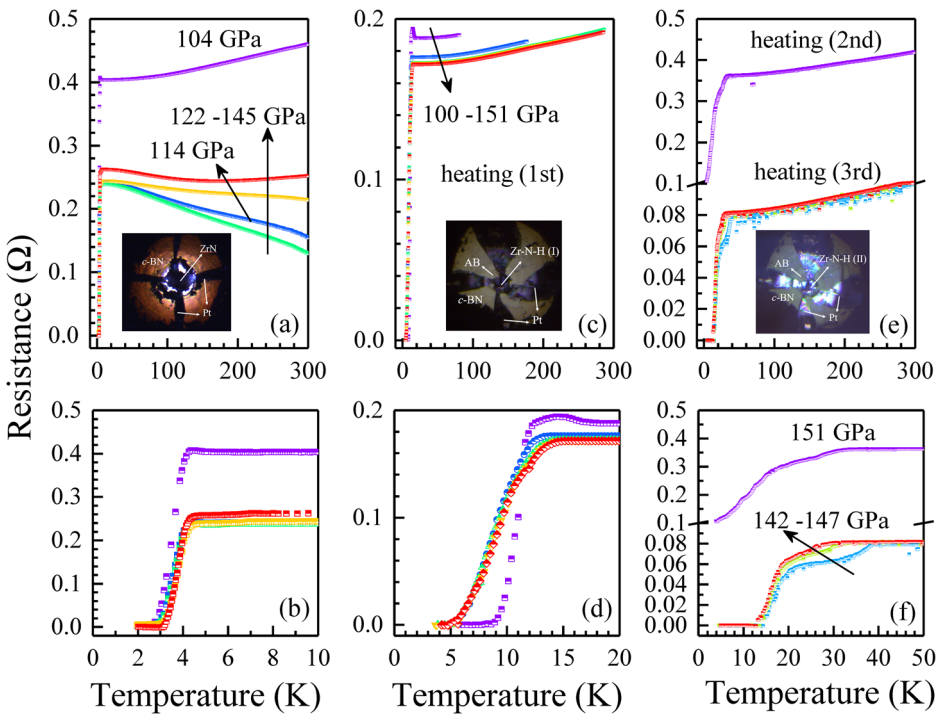

Fig. 6 | The resistance measurements. **a** Temperature dependence on the electrical resistance of ZrN at different pressures. The inset shows a microscopic image of ZrN sample in the DAC. **b** A local close-up of (**a**) in the temperature range of 0–10 K. **c** Temperature dependence on the electrical resistance of Zr-N-H at different pressures, corresponding to the first heating process. The inset shows a microscopic image of Zr-N-H (the first heating process) sample in the DAC. **d** A local close-up of (**c**) in the temperature range of 0–20 K. **e** Temperature dependence on the electrical resistance of Zr-N-H at different pressures, respectively corresponding to the second and third heating processes. The inset shows a microscopic image of Zr-N-H (the third heating process) sample in the DAC. **f** A local close-up of (**e**) in the temperature range of 0–50 K.

near 40 K at 142 GPa is also significantly higher than those of other nitrides, such as 25.5 K for electron-doped layered HfN at ambient pressure[47] and 30 K for CuN at ambient pressure[61].

Conclusions

In summary, based on the particle swarm optimization method and the first-principles calculations, we have obtained two stable Zr-N-H hydrides in the pressure range of 100–150 GPa, namely $P6_3/mmc$-$ZrNH_2$ and $F\bar{4}3m$-ZrNH. The former is a system containing H_2 quasi-molecules, while the latter contains H elements in the form of atoms. And both $P6_3/mmc$-$ZrNH_2$ and $F\bar{4}3m$-ZrNH have been predicted as superconductors. As the pressure changes, the two Zr-N-H hydrides exhibit significantly different superconducting transition temperatures. The T_c of $P6_3/mmc$-$ZrNH_2$ is approximately in the range of 15–17 K, while the T_c of $F\bar{4}3m$-ZrNH is approximately in the range of 36–40 K, both of which are significantly higher than the 4–5 K of ZrN. Furthermore, we have also successfully synthesized Zr-N-H ternary hydrides under high-pressure and laser-heating conditions. Utilizing ZrN as a precursor and introducing a hydrogen source, we have fabricated two Zr-N-H superconducting systems. The obtained resistance-temperature dependence proves superconductivity in Zr-N-H ternary hydrides different from ZrN. Combining with theoretical predictions, we have identified that in the two experimentally synthesized superconducting systems, the ternary hydride superconductor with low T_c corresponds to the $P6_3/mmc$-$ZrNH_2$ phase, while the ternary hydride superconductor with high T_c corresponds to the $F\bar{4}3m$-ZrNH phase. The maximum of T_c is about 40 K in $F\bar{4}3m$-ZrNH phase. Although the superconducting temperature of Zr-N-H still needs further optimization and improvement, our results demonstrate the superconductivity of Zr-N-H ternary hydrides from theoretical and experimental aspects, which provides a new paradigm for exploring the superconductivity of hydrides.

Methods

Computational details

For Zr-N-H system, we searched for the stable crystal structures by employing the CALYPSO[62,63] code based on the particle swarm optimization method. The structural prediction was conducted in conjunction with the VASP code[64,65]. In order to study the effect of pressure on the phase transition of structures, the CALYPSO simulations were performed at pressures of 100, 130, and 150 GPa, respectively, with the unit cell sizes ranging from 1 to 4 formula cells (f.u.). After obtaining the candidates for Zr-N-H at different pressures, all calculations of structural optimizations and electronic states were carried out by using the exchange-correlation functional of generalized gradient approximation in version of Perdew-Burke-Ernzerhof[66], as implemented in the QUANTUM-ESPRESSO (QE) code[67,68]. The cutoff energy was set as 80 Ry for wave functions. In the optimization process, convergence thresholds were set as 10^{-5} eV in total energy and 10^{-3} eV/Å in force. The k-point of the Brillouin zone was 0.02 $^{-1}$ interval distribution of Monkhorst-pack for the optimization of structures, and the k-point interval of the total energy self-consistent calculation was 0.01 $Å^{-1}$ or better.

For the stable and metallic phases of Zr-N-H, the phonon dispersion and the EPC were calculated to predict the possible superconductivity within the framework of density functional perturbation theory[69] implemented in the QE code. The PAW-type pseudopotentials for Zr, N, and H were used in QE code. The dense k-point grid of Monkhorst-Pack of $24 \times 24 \times 24$ and an irreducible q-point grid of $6 \times 6 \times 6$ were used in the calculation of the electron-phonon interaction matrix element. Based on the calculated phonon frequency (ω) and the Eliashberg electron-phonon spectral function [$\alpha^2F(\omega)$], the electron-phonon coupling constant (λ, EPC) of the hydride was calculated, which is defined by integration over the entire frequency domain of $\alpha^2F(\omega)$:

$$\lambda = 2\int_0^\infty \frac{\alpha^2F(\omega)}{\omega}d\omega. \quad (1)$$

Then T_c was calculated by Allen-Dynes-corrected McMillan eq.[57]

$$T_c = f_1 f_2 \frac{\omega_{\log}}{1.2}\exp\left[-\frac{1.04(1+\lambda)}{\lambda-\mu^*(1+0.62\lambda)}\right], \quad (2)$$

where the factor f_1f_2 is decided by the λ, $\mu^\star$, $\omega_{\log}$, and mean square frequency ($\overline{\omega_2}$)[57], and the logarithmic average of phonon frequency $\omega_{\log}$ is written as:

$$\omega_{\log} = \exp\left[\frac{2}{\lambda}\int_0^\infty \frac{\alpha^2F(\omega)\log(\omega)}{\omega}d\omega)\right]. \quad (3)$$

Considering the relatively low hydrogen content in Zr-N-H here, we took the Coulomb pseudopotential $\mu^\star = 0.15$.

Material preparation and measurements

Hydrides were synthesized by using a series of symmetric DACs. The type-Ia diamonds with 80 μm culets, single beveled to 300 μm were used for all the measurements. Ammonia borane (NH_3BH_3) was selected as the hydrogen source due to its decomposition reaction upon heating[11]. NH_3BH_3 was purchased from Aladdin, with a purity of 97%. ZrN with NaCl-type structure was purchased from MACKLIN, with a purity of 99.9%. The sample chamber with the diameter of 50 μm was made by the T301 steel. The mixture of cubic boron nitride (c-BN) and epoxy resin was put on the one surface of the chamber to provide the insulation. The ZrN sample was pressed into 2 μm thin sheets. The sample sheet was cut with the size of ~$30 \times 30 \times 5$ μm^3 and then loaded along with NH_3BH_3 into the chamber inside the argon glovebox. The volume ratio of ZrN to NH_3BH_3 was not controlled during the experiments. The added excess NH_3BH_3 into the sample cavity ensures that sufficient hydrogen gas can be generated to react with ZrN after the laser heating. To compare the results of possibly synthesized Zr-N-H, we loaded the ZrN sample into the sample chamber of a DAC without the use of any pressure medium. A standard four-probe method was used for the electrical transport measurements. Raman spectra of the first-order diamond edge were utilized to determine the pressure[70]. Raman scattering experiments were performed with the laser excitation at a wavelength of 488 nm using backscattering geometry.

Data availability

The data that support the findings of this study have been included in the plotted figures and listed tables in the main text. If any additional information or any extra data will be required in order to reproduce the results reported in this work, please contact the corresponding author.

Received: 7 November 2024; Accepted: 17 April 2025;
Published online: 24 April 2025

References

1. Chen, X. J. et al. Pressure-induced metallization of silane. *Proc. Natl. Acad. Sci. USA* **105**, 20 (2008).
2. Chen, X. J. et al. Superconducting behavior in compressed solid SiH_4 with a layered structure. *Phys. Rev. Lett.* **101**, 077002 (2008).
3. Li, Y. et al. Superconductivity at ~100 K in dense $SiH_4(H_2)_2$ predicted by first principles. *Proc. Natl. Acad. Sci. USA* **107**, 15708 (2010).
4. Zhong, G. H. et al. Structural, electronic, dynamical, and superconducting properties in dense $GeH_4(H_2)_2$. *J. Phys. Chem. C* **116**, 5225 (2012).
5. Cheng, Y. et al. Pressure-induced superconductivity in H_2-containing hydride $PbH_4(H_2)_2$. *Sci. Rep.* **5**, 16475 (2015).
6. Duan, D. et al. Pressure-induced metallization of dense $(H_2S)_2H_2$ with high-T_c superconductivity. *Sci. Rep.* **4**, 6968 (2014).
7. Drozdov, A. P., Eremets, M. I., Troyan, I. A., Ksenofontov, V. & Shylin, S. I. Conventional superconductivity at 203 kelvin at high pressures in the sulfur hydride system. *Nature* **525**, 73 (2015).

8. Liu, H., Naumov, I. I., Hoffmann, R., Ashcroft, N. W. & Hemley, R. J. Potential high-T_c superconducting lanthanum and yttrium hydrides at high pressure. *Proc. Natl. Acad. Sci. USA* **114**, 6990 (2017).
9. Peng, F. et al. Hydrogen clathrate structures in rare earth hydrides at high pressures: possible route to room-temperature superconductivity. *Phys. Rev. Lett.* **119**, 107001 (2017).
10. Drozdov, A. P. et al. Superconductivity at 250 K in lanthanum hydride under high pressures. *Nature* **569**, 528 (2019).
11. Somayazulu, M. et al. Evidence for superconductivity above 260 K in lanthanum superhydride at megabar pressures. *Phys. Rev. Lett.* **122**, 027001 (2019).
12. Bhattacharyya, P. et al. Imaging the Meissner effect in hydride superconductors using quantum sensors. *Nature* **627**, 73 (2024).
13. Wang, H., Tse, J. S., Tanaka, K., Iitaka, T. & Ma, Y. Superconductive sodalite-like clathrate calcium hydride at high pressures. *Proc. Natl. Acad. Sci. USA* **109**, 6463 (2012).
14. Li, Y. et al. Pressure-stabilized superconductive yttrium hydrides. *Sci. Rep.* **5**, 9948 (2015).
15. Kvashnin, A. G., Semenok, D. V., Kruglov, I. A., Wrona, I. A. & Oganov, A. R. High-temperature superconductivity in a Th-H system under pressure conditions. *ACS Appl. Mater. Interfaces* **10**, 43809 (2018).
16. Semenok, D. V., Kvashnin, A. G., Kruglov, I. A. & Oganov, A. R. Actinium hydrides AcH_{10}, AcH_{12}, and AcH_{16} as high-temperature conventional superconductors. *J. Phys. Chem. Lett.* **9**, 1920 (2018).
17. Hai, Y. L. et al. Cage structure and near room-temperature superconductivity in TbH_n (n = 1–12). *J. Phys. Chem. C* **125**, 3640 (2021).
18. Zhong, X. et al. Prediction of above-room-temperature superconductivity in lanthanide/actinide extreme superhydrides. *J. Am. Chem. Soc.* **144**, 13394 (2022).
19. Semenok, D. V. et al. Superconductivity at 161 K in thorium hydride ThH_{10}: synthesis and properties. *Mater. Today* **33**, 36 (2020).
20. Troyan, I. A. et al. Anomalous high-temperature superconductivity in YH_6. *Adv. Mater.* **33**, 2006832 (2021).
21. Kong, P. P. et al. Superconductivity up to 243 K in the yttrium-hydrogen system under high pressure. *Nat. Commun.* **12**, 5057 (2021).
22. Chen, W. et al. High-temperature superconducting phases in cerium superhydride with a T_c up to 115 K below a pressure of 1 Megabar. *Phys. Rev. Lett.* **127**, 117001 (2021).
23. Ma, L. et al. High-temperature superconducting phase in clathrate calcium hydride up to 215 K at a pressure of 172 GPa. *Phys. Rev. Lett.* **128**, 167001 (2022).
24. Li, Z. et al. Superconductivity above 200 K discovered in superhydrides of calcium. *Nat. Commun.* **13**, 2863 (2022).
25. Sun, D. et al. High-temperature superconductivity on the verge of a structural instability in lanthanum superhydride. *Nat. Commun.* **12**, 6863 (2021).
26. Flores-Livas, J. A. et al. A perspective on conventional high-temperature superconductors at high pressure: methods and materials. *Phys. Rep.* **856**, 1 (2020).
27. Amsler, M. Thermodynamics and superconductivity of $S_xSe_{1-x}H_3$. *Phys. Rev. B* **99**, 060102(R) (2019).
28. Guan, H., Sun, Y. & Liu, H. Superconductivity of H_3S doped with light elements. *Phys. Rev. Res.* **3**, 043102 (2021).
29. Hai, Y. L. et al. Prediction of high-T_c superconductivity in H_6SX (X = Cl, Br) at pressures below one megabar. *Phys. Rev. B* **105**, L180508 (2022).
30. Niu, R. et al. Structures and low-pressure high-temperature superconductivity of a SB-based hydride SBH_7. *J. Phys. Chem. C* **127**, 20169 (2023).
31. Semenok, D. V. et al. Superconductivity at 253 K in lanthanum-yttrium ternary hydrides. *Mater. Today* **48**, 18 (2021).
32. Bi, J. et al. Giant enhancement of superconducting critical temperature in substitutional alloy $(La,Ce)H_9$. *Nat. Commun.* **13**, 5952 (2022).
33. Chen, W. et al. Enhancement of superconducting properties in the La-Ce-H system at moderate pressures. *Nat. Commun.* **14**, 2660 (2023).
34. Chen, L. C. et al. Synthesis and superconductivity in yttrium-cerium hydrides at high pressures. *Nat. Commun.* **15**, 1809 (2024).
35. Huang, G. et al. Synthesis of superconducting phase of $La_{0.5}Ce_{0.5}H_{10}$ at high pressures. *J. Phys. Condens. Matter.* **36**, 075702 (2024).
36. Di Cataldo, S., Heil, C., von der Linden, W. & Boeri, L. $LaBH_8$: Towards high-T_c low-pressure superconductivity in ternary superhydrides. *Phys. Rev. B* **104**, L020511 (2021).
37. Liang, X. et al. Prediction of high-T_c superconductivity in ternary lanthanum borohydrides. *Phys. Rev. B* **104**, 134501 (2021).
38. Gao, M., Yan, X. W., Lu, Z. Y. & Xiang, T. Phonon-mediated high-temperature superconductivity in the ternary borohydride KB_2H_8 under pressure near 12 GPa. *Phys. Rev. B* **104**, L100504 (2021).
39. Li, S., Wang, H., Sun, W., Lu, C. & Peng, F. Superconductivity in compressed ternary alkaline boron hydrides. *Phys. Rev. B* **105**, 224107 (2022).
40. Jiang, M. J. et al. High-temperature superconductivity below 100 GPa in ternary C-based hydride MC_2H_8 with molecular crystal characteristics (M = Na, K, Mg, Al, and Ga). *Phys. Rev. B* **105**, 104511 (2022).
41. Ming, X. et al. Absence of near-ambient superconductivity in $LuH_{2x}N_y$. *Nature* **620**, 72–77 (2023).
42. Fang, Y.-W., Dangić, D. & Errea, I. Assessing the feasibility of near-ambient conditions superconductivity in the Lu-N-H system. *Commun. Mater.* **5**, 61 (2024).
43. Zhao, X. et al. Possible superconductivity transition in nitrogen-doped lutetium hydride observed at megabar pressure. *Adv. Sci.* **12**, 2409092 (2025).
44. Wan, Z. & Zhang, R. Metallization of hydrogen by intercalating ammonium ions in metal fcc lattices at lower pressure. *Appl. Phys. Lett.* **121**, 192601 (2022).
45. Spengler, W., Kaiser, R., Christensen, A. N. & Müller-Vogt, G. Raman scattering, superconductivity, and phonon density of states of stoichiometric and nonstoichiometric TiN. *Phys. Rev. B* **17**, 1095 (1978).
46. Christensen, A. N., Dietrich, O. W., Kress, W. & Teuchert, W. D. Phonon anomalies in transition-metal nitrides: ZrN. *Phys. Rev. B* **19**, 5699 (1979).
47. Yamanaka, S., Hotehama, K. I. & Kawaji, H. Superconductivity at 25.5 K in electron-doped layered hafniumnitride. *Nature* **392**, 580 (1998).
48. Chen, X. J. et al. Pressure-induced phonon frequency shifts in transition-metal nitrides. *Phys. Rev. B* **70**, 014501 (2004).
49. Chen, X. J. et al. Hard superconducting nitrides. *Proc. Natl. Acad. Sci. USA* **102**, 3198 (2005).
50. Chhowalla, M. & Unalan, H. E. Thin films of hard cubic Zr_3N_4 stabilized by stress. *Nat. Mater.* **4**, 317 (2005).
51. Chen, F. et al. Emergence of superconducting dome in ZrN_x films via variation of nitrogen concentration. *Sci. Bull.* **68**, 674 (2023).
52. Kinoshita, K. Crystal structures and properties of superconducting materials I. *Phase Transit.* **23**, 73 (1990).
53. Palanivel, B., Kalpana, G. & Rajagopalan, M. Band structure and superconductivity of ZrN under high pressure. *J. Alloy. Compd.* **202**, 51 (1993).
54. Lu, W., Zhai, H., Li, Q. & Chen, C. Pronounced enhancement of superconductivity in ZrN via strain engineering. *J. Phys. Chem. Lett.* **12**, 1985 (2021).
55. Pickard, C. J. & Needs, R. J. Structure of phase III of solid hydrogen. *Nat. Phys.* **3**, 473 (2007).
56. Ojha, P., Aynyas, M. & Sanyal, S. P. Pressure-induced structural phase transformation and elastic properties of transition metal mononitrides. *J. Phys. Chem. Solid* **68**, 148 (2007).
57. Allen, P. B. & Dynes, R. C. Transition temperature of strong-coupled superconductors reanalyzed. *Phys. Rev. B* **12**, 905 (1975).
58. Zhao, W. et al. Pressure induced clathrate hydrogen-rich superconductors KH_{20} and KH_{30}. *Inorg. Chem.* **61**, 18112 (2022).

59. Yao, S., Wang, C., Liu, S., Jeon, H. & Cho, J. H. Formation mechanism of chemically precompressed hydrogen clathrates in metal superhydrides. *Inorg. Chem.* **60**, 12934 (2021).
60. Wang, J. et al. High-T_c superconductivity of polyhydride Rb_2MgH_{18} with a layered hydrogen structure at high pressure. *J. Mater. Chem. C* **11**, 14755 (2023).
61. Liao, Z. W., Yi, X. W., You, J. Y., Gu, B. & Su, G. Family of binary transition metal pnictide superconductors. *Phys. Rev. B* **108**, 014501 (2023).
62. Wang, Y., Lv, J., Zhu, L. & Ma, Y. Crystal structure prediction via particle-swarm optimization. *Phys. Rev. B* **82**, 094116 (2010).
63. Wang, Y., Lv, J., Zhu, L. & Ma, Y. CALYPSO: a method for crystal structure prediction. *Comput. Phys. Commun.* **183**, 2063 (2012).
64. Kresse, G. & Furthmülle, J. Efficiency of ab-initio total energy calculations for metals and semiconductors using a plane-wave basis set. *Comput. Mater. Sci.* **6**, 15 (1996).
65. Kresse, G. & Furthmülle, J. Efficient iterative schemes for *ab* initio total-energy calculations using a plane-wave basis set. *Phys. Rev. B* **54**, 11169 (1996).
66. Perdew, J. P., Burke, K. & Ernzerhof, M. Generalized gradient approximation made simple. *Phys. Rev. Lett.* **77**, 3865 (1996).
67. Giannozzi, P. et al. QUANTUM ESPRESSO: a modular and open-source software project for quantum simulations of materials. *J. Phys. Condens. Matter* **21**, 395502 (2009).
68. Giannozzi, P. et al. Advanced capabilities for materials modelling with Quantum ESPRESSO. *J. Phys. Condens. Matter* **29**, 465901 (2017).
69. Baroni, S., De Gironcoli, S., Dal Corso, A. & Giannozzi, P. Phonons and related crystal properties from density-functional perturbation theory. *Rev. Mod. Phys.* **73**, 515 (2001).
70. Akahama, Y. & Kawamura, H. Pressure calibration of diamond anvil Raman gauge to 310 GPa. *J. Appl. Phys.* **100**, 043516 (2006).

Acknowledgements

The work was supported by the Shenzhen Science and Technology Program (Grant No. KQTD20200820113045081), the National Natural Science Foundation of China (Grant No. 12074401), and Guangdong Basic and Applied Basic Research Foundation (Grant No. 2024A1515011757). H.-Q. Lin acknowledges financial support from NSFC 12088101.

Author contributions

X.J.C., H.Q.L. and G.H.Z. conceived this project. S.A.L. and G.H.Z. carried out the theoretical calculations. T.L. L.C.C. and X.J.C. conducted the experimental synthesis and experimental measurements. X.J.C., H.Q.L., and G.H.Z. analyzed the data. G.H.Z. and X.J.C. wrote and revised the paper with the inputs from other authors. All authors discussed the results. The manuscript reflects the contributions of all authors.

Competing interests

The authors declare no competing interests.

Additional information

Supplementary information The online version contains supplementary material available at https://doi.org/10.1038/s43246-025-00808-0.

Correspondence and requests for materials should be addressed to Guo-Hua Zhong or Xiao-Jia Chen.

Peer review information *Communications Materials* thanks Yue-Wen Fang and the other, anonymous, reviewer(s) for their contribution to the peer review of this work. Primary Handling Editors: Rostislav Hrubiak and Aldo Isidori. A peer review file is available.

Reprints and permissions information is available at http://www.nature.com/reprints

Publisher's note Springer Nature remains neutral with regard to jurisdictional claims in published maps and institutional affiliations.

Open Access This article is licensed under a Creative Commons Attribution-NonCommercial-NoDerivatives 4.0 International License, which permits any non-commercial use, sharing, distribution and reproduction in any medium or format, as long as you give appropriate credit to the original author(s) and the source, provide a link to the Creative Commons licence, and indicate if you modified the licensed material. You do not have permission under this licence to share adapted material derived from this article or parts of it. The images or other third party material in this article are included in the article's Creative Commons licence, unless indicated otherwise in a credit line to the material. If material is not included in the article's Creative Commons licence and your intended use is not permitted by statutory regulation or exceeds the permitted use, you will need to obtain permission directly from the copyright holder. To view a copy of this licence, visit http://creativecommons.org/licenses/by-nc-nd/4.0/.

© The Author(s) 2025